Novel HIPIMS deposited nanostructured CrN/NbN coatings for environmental protection of steam turbine components

HOVSEPIAN, Papken <http://orcid.org/0000-0002-1047-0407>, EHIASARIAN, Arutiun <http://orcid.org/0000-0001-6080-3946>, PURANDARE, Yashodhan <http://orcid.org/0000-0002-7544-9027>, MAYR, Peter, ABSTOSS, Kevin, MOSQUERAFEIJOO, Maria, SCHULZ, Wencke, KRANZMANN, Axel, LASANTA, Maria and TRUJILLO, Javier

Novel HIPIMS deposited nanostructured CrN/NbN coatings for environmental protection of steam turbine components.

P. Eh. Hovsepian [a*], A. P. Ehiasarian [a], Y. P. Purandare [a], P. Mayr [b], K. G. Abstoss [b], M. Mosquera Feijoo [c], W. Schulz [c], A. Kranzmann [c], M.I. Lasanta [d], J.P-Trujillo [d]

[a] *UK National HIPIMS Technology Centre, Materials and Engineering Research Institute, Howard Street, Sheffield Hallam University, Sheffield, S1 1WB, UK.*

[b] *Welding Engineering Institute of Joining and Assembly, Technische Universität Chemnitz, Reichenhainer Strasse 70, 09126 Chemnitz, Germany*

[c] *BAM, Federal Institute for Materials Research and Testing, Unter den Eichen 87 12205 Berlin, Germany.*

[d] *Grupo de Investigación Ingeniería de Superficies y Materiales Nanoestructurados, Facultad de Ciencias Químicas, Universidad Complutense de Madrid, Spain*

* Corresponding author: Email: P.Hovsepian@shu.ac.uk. Telephone: +44-114-225 3644 Fax: +44-114-225 3501.

Abstract

To increase efficiency, modern steam plants are pushing their operational regime from super-critical (600°C/300 bar) to ultra- super-critical (740/760°C/350 bar) stretching existing turbine materials to their limits. The focus is on new generation functional materials and technologies which complement the inherent properties of existing materials.

Current work proposes a novel High Power Impulse Magnetron Sputtering (HIPIMS) deposition technology, for the first time, for deposition of a ceramic based CrN/NbN coating with a nanoscale multilayer structure (bi-layer thickness Δ = 1.9 nm) with superior adhesion (L_{C2}= 80N) to protect low Chromium P92 steel widely used in steam power plants. Thermodynamic calculations predict the equilibrium phases and aggressive gaseous compounds generated by the interaction of steam with the coating. CrN/NbN coated P92 steel

samples oxidised at 600°C in a high pressure (50 bar) 100% steam atmosphere for up to 1000 h reveal the coating's superior oxidation resistance and protective mechanisms, especially against the detrimental effect of Hydrogen. High temperature (650°C) Tensile Strength, Low Cycle Fatigue and Creep tests confirm that, unlike other state-of-the-art PVD technologies, HIPIMS is not detrimental to the mechanical properties of the substrate material. Water droplet erosion tests confirm no measurable weight loss after 2.4×10^6 impacts.

Keywords: hipims; CrN/NbN; nanoscale multilayers; steam oxidation resistance; water droplet erosion resistance.

1. Introduction:

Steam-powered turbines employ the Carnot cycle, whose efficiency is defined as $\frac{T_{max}-T_{min}}{T_{max}}$, *where* T_{max} is the maximum temperature in the thermodynamic cycle and T_{min} is the minimum temperature, both as absolute temperatures. Therefore, the most natural route to increasing the efficiency of the turbines is to use temperatures in excess of 600°C, conditions known as super-critical. A further efficiency increase can be achieved by raising the steam pressure to move from a super-critical (600°C/300bar) to an ultra- super-critical (740/760°C/350bar) regime of operation [1].

However, the high temperature/ high pressure steam atmosphere is extremely aggressive with corrosion fatigue, stress corrosion cracking, erosion corrosion and steam oxidation identified as the main surface degradation mechanisms acting in steam turbines. The challenge for material selection becomes even higher for the turbine blades, which have to withstand both

high mechanical loads due to high rotation speeds and environmental attack due to the elevated temperature.

It has become increasingly more difficult to develop a turbine blade alloy with the right balance of properties of creep rupture and fatigue strength, environmental resistance and microstructural stability. In general, blade failures can be grouped into two categories: (a) fatigue, including both high (HCF) and low cycle fatigue (LCF) and (b) creep rupture [2, 3, 4]. Blade fatigue failures are often related to anomalies in mechanical behaviour and manufacturing defects such as machining marks, poor surface finish, initial flaws or heat treatment. In such complex degradation conditions where both the surface and bulk of the component are subjected to a severe attack during exploitation, the application of coatings provides a natural alternative route representing a composite structure where the bulk and surface properties can be tailored separately to achieve high performance. In this scenario, the physical vapour deposition (PVD) coating technique can be very useful in depositing oxidation resistant coatings and therefore mitigating surface degradation problems due to environmental attack. This technique has an advantage that coatings of a wide variety of elements in either their pure or compound form (nitrides, carbides, oxides or combination of all these) can be deposited.

However, the application of coatings to the blade material often has further mechanical side effects, which can lead to the premature failure of coated components via low-cycle fatigue (LCF) and thermo-mechanical fatigue (TMF). In most cases the mismatch in the properties of the coating and the substrate alloy are responsible for exacerbating the failure mechanism. The mismatch may arise due to differences in the thermal expansion coefficients, ductility, strength and elastic moduli [5]. Furthermore, coating morphology, density and microstructure can significantly influence surface crack initiation and its propagation and thus influence the

fatigue life of the coated component. With the introduction of the novel High Power Impulse Magnetron Sputtering (HIPIMS) technique, very dense and defect free coatings with high adhesion can be deposited [6]. HIPIMS utilises transient impulse (short pulses) glow discharge with a very high power and current density (up to 3 $kW \cdot cm^{-2}$ and 4 $A \cdot cm^{-2}$ respectively, at a duty cycle of < 5%) which translates to high plasma densities and ionised metal particles [7]. The utilisation of highly ionised metal fluxes during the surface pre-treatment and coating deposition stages allow fine-tuning of the metallurgical reactions at the coating substrate interface as well as precise control over the coating structure, crystallographic orientation, and surface morphology.

To benefit from these advantages, HIPIMS technology has been employed in a deposition process to produce nanostructured coating for the protection of steam turbine blades. It is also worth mentioning that the concept of utilising the synergy between two nitrides in a nanoscale multilayer structure in CrN/NbN coating is new in the steam turbine application field. Therefore, the motivation behind the reported research is to investigate and reveal the barrier properties of the novel nanostructured CrN/NbN coating in a steam environment where it is exposed to high temperature oxidation and water droplet erosion and elucidate the effect of the new coating and technology on the mechanical properties of the bulk blade material.

It was reported previously that in a steam free environment, HIPIMS deposited CrN/NbN nanoscale multilayer coatings exhibited excellent room temperature wet corrosion resistance, wear resistance [8, 9] and tribo-corrosion resistance [10]. Their superior wear and corrosion resistance was attributed to the presence of high hardness Me-nitrides of relatively electrochemically inert elements such as Cr and Nb [8]. Moreover the coatings were found to possess superior oxidation resistance up to a temperature range of 820 - 850 °C depending on the stoichiometry of the coatings (N/Me ratio) [11]. The aqueous corrosion resistance of Nb is

well known whereas literature suggests that the oxidation behaviour of Nb is very complex. It can provide some oxidation resistance in the temperature range of 600 -1000 °C because of its refractory nature [12] (provided that the oxide scales (Nb_20_5) remain attached with the base material) or because of its low porosity [13].

In a previous study, HIPIMS deposited CrN/NbN multilayer coatings showed excellent performance when exposed to 650 °C in a low pressure (1bar), pure steam environment [14]. The coating contained a higher concentration (atomic %) of Cr as compared to Nb (N: Cr: Nb = 57.96: 29.87: 12.17). Substrates (P92) coated with this composition exhibited two orders of magnitude lower weight gain as compared to uncoated substrates even after 2000 hours of testing. However, the oxidation kinetics is expected to be influenced both, by the coating composition (Cr/Nb ratio) and the steam pressure. This study aims at understanding the effect of these two parameters on the oxidation resistance. To this end, CrN/NbN coatings with a higher Nb content have been deposited by the HIPIMS technique. Furthermore, oxidation and droplet erosion tests have been carried out at significantly higher steam pressure of 50 bar. The paper presents detailed results of this new research.

2. Experimental Details:

2.1 *Coating Deposition*

Nanoscale multilayer CrN/NbN coatings have been deposited on P92 steel in a conventional industrial Unbalanced Magnetron Sputtering (UBM) machine (HTC 1000-4, four-cathode system (Hauzer Techno Coatings, Europe B.V., Venlo, The Netherlands) enabled with HIPIMS technology. The HIPIMS plasma was generated using dedicated Highpulse 4008 power supplies (Hüttinger Elektronik Sp. z o.o., Warsaw, Poland). The deposition was carried out using two pairs of Cr and Nb targets, whilst the substrates were subjected to heating, three-fold rotation and DC bias. Details of the deposition system such as target arrangement,

substrate holder and general information on coating deposition parameters as well as multilayer coating scheme can be found in the previous publication [14].

In order to characterise the coatings extensively, various types of test coupons were coated. For XRD and TEM analysis coatings deposited on 1-micron finish 304L stainless steel substrates were used whereas mechanical and tribological properties were evaluated on 1-micron finish HSS coated specimens. For oxidation studies coatings were deposited on P92 steel substrates which had an engineering surface finish i.e. surfaces with deep grinding marks (Ra value of 0.63 μm). Irrespective of the type of test coupon and surface finish, all the coupons were subjected to an adhesion enhancing HIPIMS Cr ion etching [15], followed by a CrN base layer deposition and bulk coating deposition consisting of alternating nanoscale CrN and NbN layers.

For a CrN/NbN multilayer coating deposited at a fixed total chamber pressure, relative atomic percentage of Cr in CrN as well as Nb in NbN (N/Me and Cr/Nb ratios) will depend on the power applied on the cathodes furnished with Cr and Nb targets respectively. In order to increase the Nb content in the films the powers on the Nb and Cr cathodes were adjusted accordingly. The deposition temperature was maintained at 400 °C whereas the bias voltage (U_b) was maintained at -65 V. In order to investigate the effect of the Cr and Nb content in the film on its performance, coatings with different Cr/Nb ratio were deposited namely: Cr rich, (Cr/Nb = 2.44): stoichiometry (N: Cr: Nb = 57.96 : 29.87 : 12.17) and Nb rich, (Cr/Nb = 1.16): stoichiometry (N: Cr: Nb = 51.38 : 26.17 : 22.45).

2.2 ***Coating Characterisation***

The coatings were characterised using a number of analytical techniques. Scanning Electron Microscopy (FEI NOVA-NANOSEM 200 and Zeiss Supra 55VP), Focused Ion Beam SEM

(Quanta 200 3D) were used to analyse the coating microstructures, whereas low-angle (2θ, 1°-10°) Bragg-Brentano geometry X-Ray Diffraction (XRD) technique was used to measure the bi-layer period of these coatings (PHILIPS XPERT). The texture of the nanoscale multilayer structure was investigated using Brag-Brentano geometry (2θ, 20-100°) XRD, using glancing angle (2° incidence) and θ-2θ geometries. The coating samples were analysed by XRD after exposure using a Bruker AXS D8 Discover. A transmission electron microscope (Philips STEM420 equipped with a LaB_6 filament) was used to analyse the multilayer structure in detail. The column boundary density was studied by high resolution transmission electron microscopy (HRTEM) in JEOL 3010 microscope interfaced with a GATAN TRIDIEM image filter.

Coating adhesion was measured by the Daimler Benz Rockwell indentation test, as well as a progressive loading scratch test conducted on CSEM-Anton Paar REVETEST. The instrumental hardness of the coatings was measured with a CSM-Anton Paar nano-hardness tester using a maximum load of 20 mN.

Steam oxidation test were carried out on CrN/NbN coated P92 steel samples in a pure steam environment using a NABERTHERM R100/750/12 furnace with a ceramic tube reactor. The tests were performed at 600^{o}C for 1000 h with a gas flow of 1.0133ms^{-1} and 50 bar overpressure.

In order to evaluate the mechanical properties of the coating fatigue, creep and tensile tests were carried out at a typical exposure temperature on coated samples as well as uncoated P92 base material. The uniaxial creep tests were performed at 650 °C and a constant stress of 120 MPa according to ASTM E139 using a vertical dead-weight creep testing machine. The creep strain was measured during the test to evaluate the influence of coating procedure on the creep behavior. Strain controlled low cycle fatigue (LCF) tests were performed according to

the ASTM E606-04 in order to test the resistance to fatigue at 650 °C. The corresponding tests were performed at a strain level of 0. 4 % and a strain rate of 3 x 10^{-3} ls^{-1} with the use of a *PowerSwing* fatigue machine by SincoTec. In addition tensile tests were carried out at 650 °C and a constant strain rate of 0.010 M per minute according to the ASTM E8. A Hegewald & Peschke machine *inspect 150* was used to perform the tensile tests. The droplet erosion test was carried out on a specialised test rig from FRT Germany producing 300 impacts per minute at water pressure of 9 bar. The impact crater was analysed by 3D-profiling and SEM imaging.

3.0 Results and Discussion:

3.1*Coating Crystallographic Structure, Morphology and Microstructure*

The crystallographic structure and architecture of the CrN/NbN have been studied by Low-angle and Bragg-Brentano XRD analyses. Figure 1a shows low angle (1°-10°, 2θ) XRD patterns for the coatings with high and low Nb content. The peaks at 2θ = 4.46° and 2.95° indicate that both coatings have a clear nanoscale multilayer structure. It also allows calculation of the bi-layer thickness Δ of the multilayer stack (thickness of a consecutive CrN and NbN layer together) using Bragg's equation. Calculations revealed that the high Nb containing coating has a bi-layer thickness of Δ= 1.97 nm whereas the coating with low Nb has Δ= 2.9 nm. This result is consistent with a difference in the sputtering yields, at 600eV of Nb and Cr, 1.3 and 0.65 respectively, [16] and the selected power values dissipated on the magnetrons during the coating deposition step of the process.

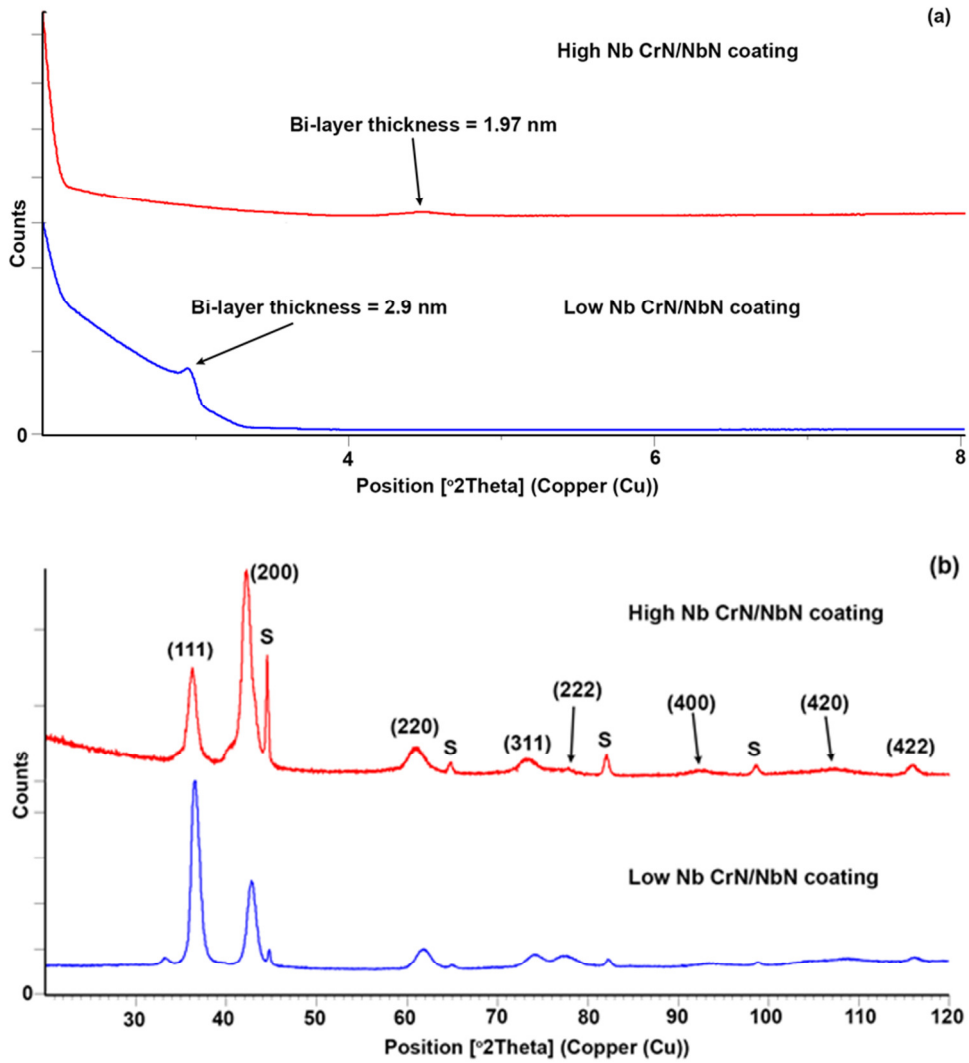

Figure 1: X-ray diffraction patterns of the CrN/NbN coatings (a) LAXRD pattern used for calculation of the bi-layer period. (b) Bragg-Brentano θ-2θ scan results.

Bragg-Brentano (θ-2θ scan) XRD measurements revealed that the coatings have a NaCl type face-centred cubic (f.c.c) structure, Figure 1b. The XRD pattern is typical for nanoscale multilayer coatings where a single reflection appears at a spacing that is a weighted mean of the individual lattice spacing for CrN and NbN. As evident from the XRD pattern, the high Nb coating has a (200) preferred orientation.

Compared to the XRD results of low Nb CrN/NbN coating, as reported previously [14] which has a (111) texture, the increase of the Nb content in the film has resulted in a texture change.

It is well understood that increased ion bombardment of the films during their growth leads to increased ad-atom mobility and thereby to changes in the coating microstructure and importantly, its preferred growth orientation. For example, it was found that the texture of CrN changed from (111) to (220) as a result of increased ion bombardment from the depositing flux (increase both in ion energy as well as ion flux bombarding the growing film) [17]. A similar shift in peak intensity (from (110) to (100)) as a result of high energy ion bombardment has been reported also for CrN/NbN multilayer coatings deposited by conventional magnetron sputtering [18].

Furthermore, it was found that the preferred texture is strongly influenced by the atomic weight of the coating elements. It was reported that when the coatings involve lighter elements (atomic weight $\leq$ 52) in dominant proportions, for example Cr-rich nitride multilayers, the texture will change from strain energy dominant (110) to surface energy dominant (100) if surface energy is sufficiently large to cause continuous re-nucleation and suppression of the competitive growth mechanism [19]. Thus the dominant (111) orientation for the low Nb CrN/NbN multilayer, which is achieved even at a low bias voltage of -65 V, can be attributed to an increased surface energy brought about by the highly mobile ad-atoms due to the persistent low energy bombardment from the HIPIMS plasma.

The effects of the surface energy and re-nucleation are more pronounced when the heavier elements (atomic weight > 52) are involved in the coating [19]. As both the CrN/NbN multilayer coatings (with high and low Nb content) are deposited in conditions with similar ion bombardment, the preferred (100) texture of the CrN/NbN with high Nb content reported in this paper can be attributed to the higher concentration of the heavier element (Nb, atomic weight $\approx$ 93) in the multilayers. Additionally, the relative increase in Nb content results in a total ion flux containing a higher proportion of Nb. The large size of the Nb ion limits its

subplantation depth and distributes its energy close to the surface. The weight contributes to a greater total energy delivered to the surface. Both these factors contribute to higher surface mobility and favour a lower surface energy surface such as the (100).

Detailed SEM analysis on the high Nb content coatings deposited on P92 samples showed the coating to be very dense in spite of the substrate surface being very rough. Figure 2a shows the SEM image of the coating morphology obtained in secondary electron imaging mode. The PVD coating technique, being a line of sight process, replicates the surface topography, in this case the grooved nature of the substrate after grinding. However, the coating, despite being deposited on a rough surface, appears very dense with fine-grained-dome shaped column tops and uniform coverage. The persistent and intentional ion bombardment of the depositing species (due to the higher ion to neutral ratio of the depositing flux) obtained in a HIPIMS plasma leads to a higher ad-atom mobility and therefore can account for this superior coverage of surface undulations and dense grain boundaries. The true nature of the 3.5 µm coating density and specimen coverage is more evident in the cross-sectional image, figure 2b which shows a sharp step in the substrate caused by a grinding operation. The coating fills the trenching at the edge of the step and continues to grow as a fully dense layer to the ultimate thickness.

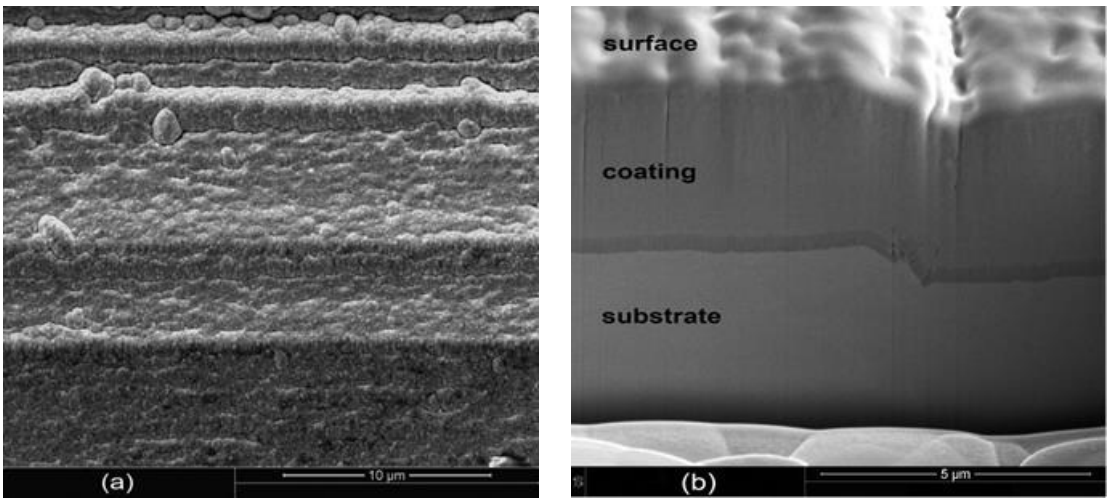

Figure 2**:** Scanning electron microscope images of CrN/NbN coating on P92 substrate: (a) surface morphology, (b) FIB cross-section image.

The microstructure of the coatings was investigated by cross section TEM analyses. Figure 3a shows a bright field STEM image of the overall CrN/NbN coating with high Nb content. As evident from the micrograph, the coating-substrate interface is extremely smooth and the coverage is free of defects caused by macro-droplet formation or uneven surface. This is typical of HIPIMS etching even though the surface is bombarded with high energy metal ions to improve adhesion. Adjacent to the substrate, a layer of CrN (around 300 nm thick) is visible which is very dense and highly textured, apparent from its appearance as a band of light contrast extending throughout its width of the cross-section.

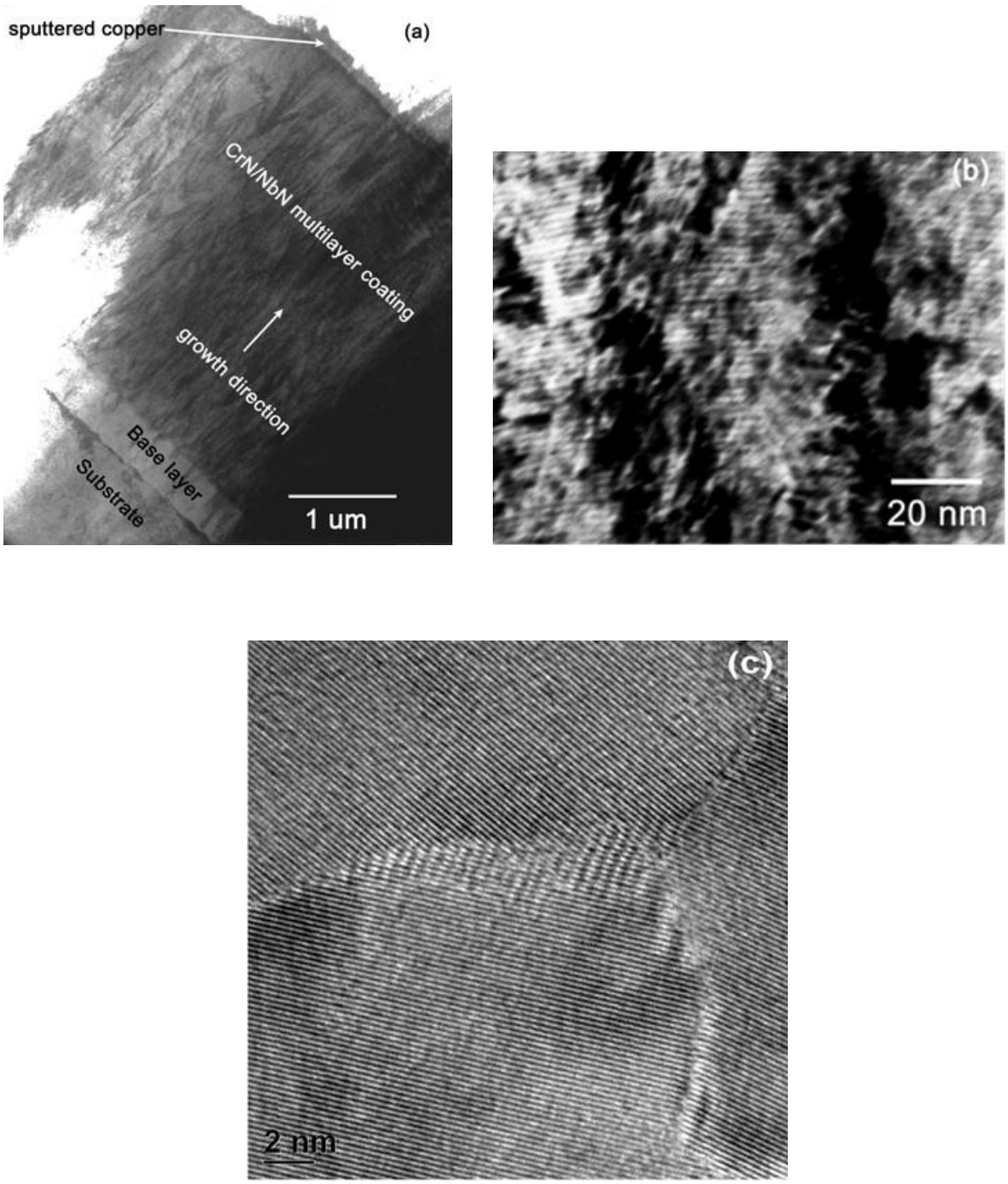

Figure 3: Bright field STEM (a) low magnification cross-section of the coating showing base layer and adjacent coating (b) high magnification showing the multilayers (c) high resolution TEM image showing the microstructure at an atomic scale [20].

The interface between the CrN base layer and the multilayer coating, similar to the base layer and substrate interface, is very smooth and uniform indicating a smooth transition of deposition conditions for the growth of multilayer structures. A glimpse of epitaxial coating

growth extending from the base layer into the multilayer coating is also visible as grains of similar contrast are seen extending upward all the way to the top of the coating along the growth direction. These coating growth features are typical of the HIPIMS technique and result in a coating with a dense microstructure [9], which in turn enhances mechanical properties such as adhesion, hardness, wear resistance [6] and corrosion resistance. This is of particular significance, as it is observed consistently irrespective of the stoichiometry of the coatings; i.e. with higher Cr content as was observed before, [9, 14] or in this case with higher Nb content. Figure 3b shows a bright field STEM image of the nanoscale multilayer structure in detail, with alternating colour contrast corresponding to alternating CrN (light coloured) and NbN (dark contrast) layers. To analyse the effect of HIPIMS on the coating density on an atomic scale, the microstructure was investigated by high resolution TEM. Figure 3c shows a plan view HRTEM image of the coating. The image shows several column boundaries with atomic rows in the adjacent columns tilted at different angles due to the different crystallographic orientation produced during coating growth. However, despite the different orientation, the atomic rows of the adjacent columns matched with good precision and no voids were visible at the column boundaries thus demonstrating very high density of the coatings.

3.2 *Coating Hardness and Adhesion*

The effect of the superior coating microstructure (dense multi-layered structure composed of hard nitrides) was thus reflected in the mechanical properties measured. The high Nb content coatings had a hardness of 27 ± 0.4 GPa and a Young's modulus of 338 ± 13 GPa whereas the low Nb content coating had a hardness of 35 ± 2 GPa and a Young's modulus of 392 ± 33 GPa. The difference in hardness values can be attributed to a combination of factors such as inherent hardness of CrN (stoichiometric CrN is intrinsically harder than NbN), difference in periodicity (bi-layer thickness) and compressive stresses in the coating. Irrespective of the

stoichiometry a high adhesion value, L_{C2} > 80 N was recorded which is a result of HIPIMS etching. Rockwell C indentation on the coated P92 substrate, irrespective of the low hardness of the substrate material, was perfectly circular without any coating de-lamination around the periphery and can be classified as Class 1 according to the Daimler-Benz adhesion test criteria.

3.3 *Thermodynamic Calculation*

Thermodynamic studies of phase equilibrium during steam oxidation processes were performed using the thermodynamic simulation tool THERMO-CALC, [21] to determine the stable phases development (namely the oxides of the metals in the coatings constitution and the various gaseous phases in the test environment), and to provide a useful approximation of the steam oxidation process. The simulations were carried out using high quality databases provided by Scientific Group Thermodata Europe such as SSUB4 for the reactions in the gaseous phases and SSOL2 for substrate definition, [22]. Those databases contain assessed thermodynamic data on enthalpy of formation, entropy and temperature dependence of the heat capacity for the gaseous and condensed compounds considered in the system studied in this work.

According to the rules of thermodynamics, for a given temperature and pressure, a system is considered to be at equilibrium when the total Gibbs free energy G, (equation 1) is at minimum.

$$G = \sum_{i=1}^{m}\left(n_i(g)\Delta G_{fi}^{0}(g) + RT\ \ln P + RT\ \ln\frac{n_i(g)}{N(g)}\right) + \sum_{i=1}^{s} n_i(s)\Delta G_{fi}^{0}(s) \quad (1)$$

where:

m , s is the number of gaseous and solid species respectively in the system

$n_{i(g)}$ and $n_{i(s)}$ are the number of mols of gaseous and solid species “i”

N(g) is the total number of mols in the gaseous phase

$\Delta G_{fi}^{0}(g), \Delta G_{fi}^{0}(s)$ are the standard free energies of formation of gaseous and solid species "*i*"

R is the gas constant.

The main input parameters for the thermodynamic calculations were the stoichiometric ratios of the coating elements, for two CrN/NbN coatings in as deposited conditions namely low Nb, (Cr/Nb = 2.44): stoichiometry (N: Cr: Nb = 57.96 : 29.87 : 12.17) and high Nb, (Cr/Nb = 1.16): stoichiometry (N: Cr: Nb = 51.38 : 26.17 : 22.45). The calculations were carried out for both coatings exposed to a pure steam atmosphere at 1bar and 50 bar pressure and temperatures in the range of 100 to 1000 ^{o}C. It was assumed that the validation atmosphere, the gas phase, steam, was always in excess in the environment.

Figure 4(a) and (b) shows the molar fraction of all stable phases developed from the low Nb CrN/NbN coating exposed to 100% steam atmosphere at 1bar and 50 bar pressure as a function of the steam temperature respectively. The thermodynamic simulation showed that for the working conditions used, the most stable phases generated from the CrN/NbN coating are Cr_2O_3 and Nb_2O_5 oxides. For both low Nb (Cr/Nb = 2.44) and high Nb (Cr/Nb = 1.16) coatings the simulation showed that the type of the solid oxide phases formed in the equilibrium conditions was identical. However, in all conditions the Cr_2O_3 oxide forms in a greater proportion. Importantly it was found that increase of the steam pressure from 1bar to 50 bar intensifies the oxidation process by factor of 10. For example, the mole fraction of Cr_2O_3 increased from 0.073 mole to 0.71 mole and Nb_2O_5 mole fraction increased from 0.043 mole to 0.426 mole when the steam pressure was increased from 1bar to 50 bar. Furthermore, the thermodynamic calculations showed that the Cr_2O_3 / Nb_2O_5 molar ratio for similar experimental conditions depends on the Cr/Nb ratio in the coating. Decrease of the Cr/Nb ratio from 2.44 to 1.16 reduces the Cr_2O_3 / Nb_2O_5 ratio from 1.755 to 0.833 thus showing that

the increase of the Nb content in CrN/NbN will lead to an increase of the relative amount of Nb_2O_5 with higher rate as compared to Cr_2O_3.

This trend was further supported by the simulations of the free Gibbs energy, ΔG required for the formation of Cr_2O_3 and Nb_2O_5 oxides as a function of the temperature. It was calculated that the Gibbs energy, ΔG for formation of Nb_2O_5, (ΔG = - 29.8 kJ/mole) is much lower when compared to that of Cr_2O_3, (ΔG = - 25.2 kJ/mole), which clearly indicates that formation of Nb_2O_2 is more favorable during steam oxidation of CrN/NbN. It was shown that ΔG for both oxides reduces with increase of the steam temperature but the trend ΔG Nb_2O_2 < ΔG Cr_2O_3 remains unchanged.

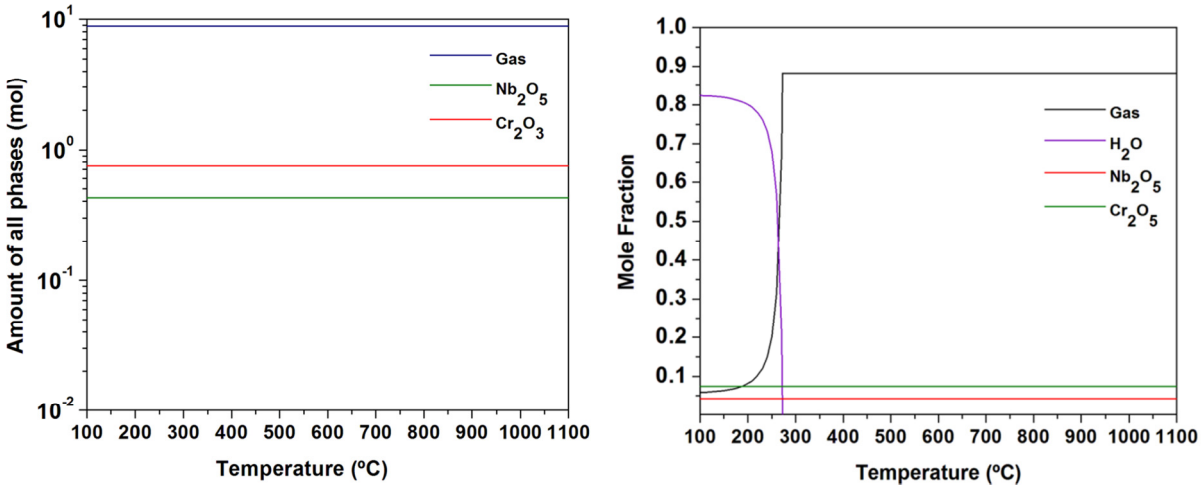

Figure 4. Main phases developed from the low Nb CrN/NbN coating exposed to 100% steam atmosphere at: (a) 1bar pressure, (b) 50 bar pressure.

The THERMO-CALC simulation provided interesting information about the various Me-oxides and gaseous hydroxide compounds formed in the working atmosphere and on the coating surface in the steam environment. These compounds form between 100ºC -1000ºC and are responsible for the material degradation process. It is important to note that in addition to the compounds, which are purely oxides, a certain amount of Hydrogen, both in

atomic and molecular form is produced, which indicates possible hydrogen inter-diffusion and therefore potential coating or even substrate material embrittlement in the course of the steam exposure.

3.4 *Steam Oxidation Behaviour*

The oxidation behaviour of CrN/NbN nanoscale multilayer coatings deposited on P92 steel substrate exposed to pure steam environment at 650^{o}C and low 1bar pressure for 2000 hours was thoroughly discussed in our previous work [14]. It was reported that the coating with higher concentration of Cr as compared to Nb, (Cr/Nb ratio of 2.44, N: Cr: Nb = 57.96: 29.87: 12.17) offers good protection against oxidation of P92. The excellent oxidation resistance of this coating was demonstrated by cross sectional SEM analyses, which showed that for the selected test conditions, the coating remained largely intact and only a 490 nm thin protective Cr_2O_3/Nb_2O_5 oxide layer was formed on the top coating surface. The coating protection mechanism can be described as one of formation of a protective top layer containing Cr and Nb oxides, effective plugging of coating voids by oxide product as well as hindered elemental transport through the coating due to the barrier properties of the interfaces between the individual nanolayers of CrN/NbN. It was shown that the coating degradation mechanism when exposed to a high temperature steam environment, although retarded and localised, was adverse diffusion of substrate elements and oxygen through coating growth defects or cracks formed due to a thermal expansion coefficient mismatch between the coating and the substrate.

The thermodynamic simulation carried out in this work contributed towards a deeper understanding of the degradation mechanism of the steam oxidation process. The simulation revealed the potentially adverse effect of higher Nb content in the film as well as the detrimental effect of the elevated steam pressure on the coating lifetime due to enhanced oxide formation rate.

To verify the predicted deterioration of the oxidation resistance of the coating due to higher Nb content by the thermodynamic simulation, a Nb rich, (Cr/Nb = 1.16): stoichiometry (N: Cr: Nb = 51.38 : 26.17 : 22.45) was exposed to a steam atmosphere of 600^{o}C at high 50 bar for 1000 hours . Glancing angle XRD analyses, (XRD pattern not shown) revealed formation of Cr_2O_3 and Nb_2O_5 as stable phases as predicted by the thermodynamic simulation. It has to be noted that the protective characteristics of the Me-oxides depend on their thermodynamic stability and mass density. The mass density of Cr_2O_3 and Nb_2O_5 are 5.22 g.cm^{-3} and 4.60 g.cm^{-3} respectively. When calculated, the specific volume of Nb_2O_5 is 12% larger than that of Cr_2O_3, which means that during the course of the oxidation process, cracks may originate in the oxide scales due to the volume expansion of the individual oxides and that this process will be dominated by the amount of the Nb_2O_5 formed.

Figure 5 shows an SEM cross-sectional image and EPMA elemental distribution map of CrN/NbN with high Nb content after the oxidation treatment. The SEM image, (see inset in the bottom-right corner of the map, Figure 5) revealed the presence of a three band (layer) oxide scale structure. The bands appear in different white/grey brightness: a top lighter grey band followed by a darker grey and a white band at the coating substrate interface. The phase composition of these three bands can be better understood when the elemental maps of Cr and N in Figure 5 are considered. The very thin white band at the interface represents the CrN base layer deposited as described in the experimental section and shown in Fig. 3a. The coating appears intact and not oxidised as, according to the elemental map for this region, no Oxygen signal was recorded. The rest of the coating however, was fully oxidised as shown by the corresponding Cr, Nb and O maps. This was also supported by the absence of Nitrogen in the corresponding map as it is well known that the mechanism of oxidation of ceramic nitride phases such as CrN and NbN consists of gradual replacement of Nitrogen with Oxygen atoms. The two grey bands seen in the SEM image can be due to different Oxygen content

deeper in the film. Importantly according to the Iron map (figure 5), there is no outward diffusion of this element in the coating, which shows that the coating provides a good degree of protection.

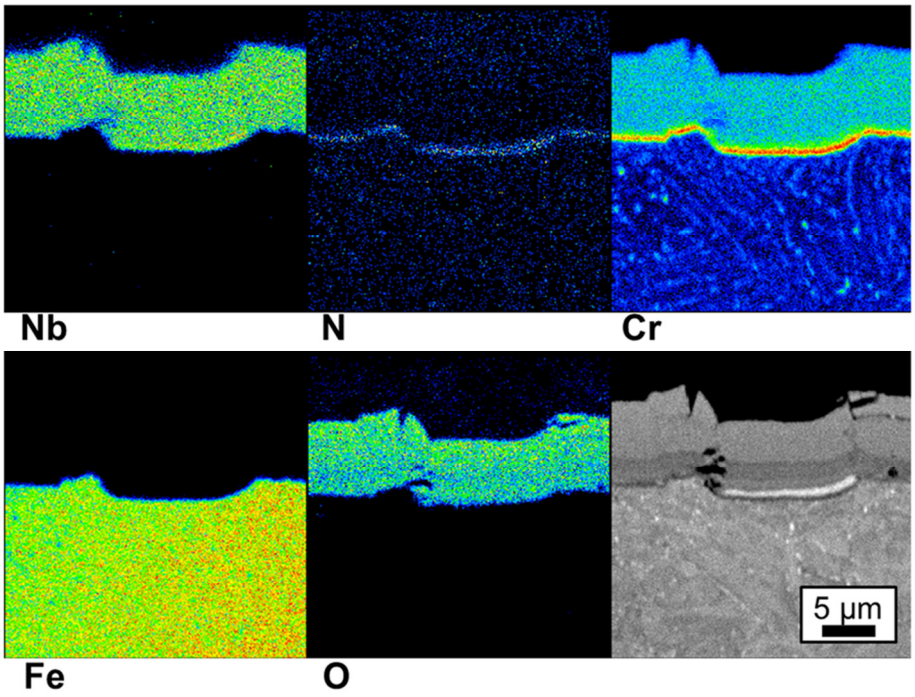

Figure 5. SEM cross-sectional image and EPMA elemental distribution map of CrN/NbN with high Nb content, Cr/Nb= 1.16 exposed to 600^{o}C pure steam atmosphere at 50 bar pressure for 1000 h.

Another interesting difference observed between the SEM cross sections of low Cr and high Nb containing CrN/NbN (images not included) was the large number of cracks in the oxidised coating observed for the high Nb containing coating. Apparently, the cracks were generated by a brittle fracture mechanism. Such cracks inevitably deteriorate the barrier properties of the coatings. One natural source for crack formation is the difference between the thermal expansion coefficients of the ceramic coating and the steel substrate material. Another possible reason for crack formation could be coating embrittlement through the incorporation

of Hydrogen from the steam environment of the test. The presence of Hydrogen in the coating was predicted by the thermodynamic calculations and is confirmed by GDOES depth profile analyses of the oxidised coating after an exposure of 2000 h, see Figure 6 (for the sake of clarity contributions from the substrate elements have been omitted in the figure). The depth profile shows that the Hydrogen content is at its maximum in the fully oxidised top layer of the coating, (see the hump in the Oxygen concentration just under 1 micrometre of depth, figure 6) and reduces towards the coating substrate interface. The GDOES depth profile for the oxidised high Nb content, (Cr/Nb = 1.16) coating, (not shown here) looks similar to that of the lower Nb content CrN/NbN coating. However, the crack damage in the oxide scale observed for the coatings with higher Nb content was more pronounced. This is believed to be due to the synergy between the Hydrogen embrittlement effect and the deeper diffusion of oxygen in these films which results in the formation of a thicker and more brittle Nb_2O_5 on the surface of these films.

The importance of this finding is that it reveals the role of Nb on the oxidation resistance of the CrN/NbN in steam atmosphere. It also shows that CrN/NbN especially with higher Cr content can act as an effective barrier to Hydrogen and oxygen diffusion and can therefore protect the substrate material from embrittlement.

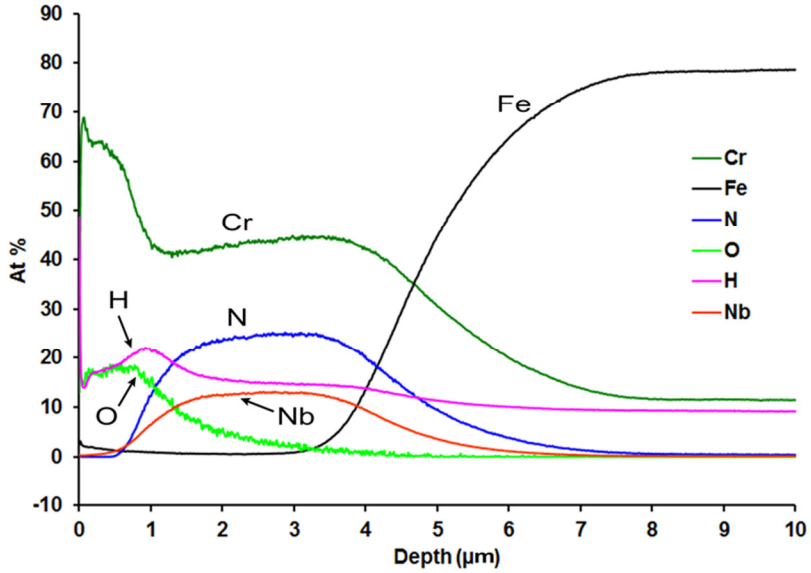

Figure 6. GDOES depth profile of steam oxidised low Nb CrN/NbN coating.

3.5 *Mechanical Behaviour*

The stress-strain curves obtained from the tensile tests conducted on the low Nb CrN/NbN coating at temperature of 650 °C are given in Figure 7a. The coated sample exhibits an ultimate tensile strength (UTS) of 307 MPa and corresponding yield strength (YS) of 291 MPa. The base material shows slightly reduced values of 229 MPa (UTS) and 222 MPa (YS). Considering the strain behaviour of the samples the base material and the coated specimen show almost identical fracture strain of 36 % and 33 %, respectively. The results indicate that coating procedure does not affect the tensile properties of the base material in a negative way.

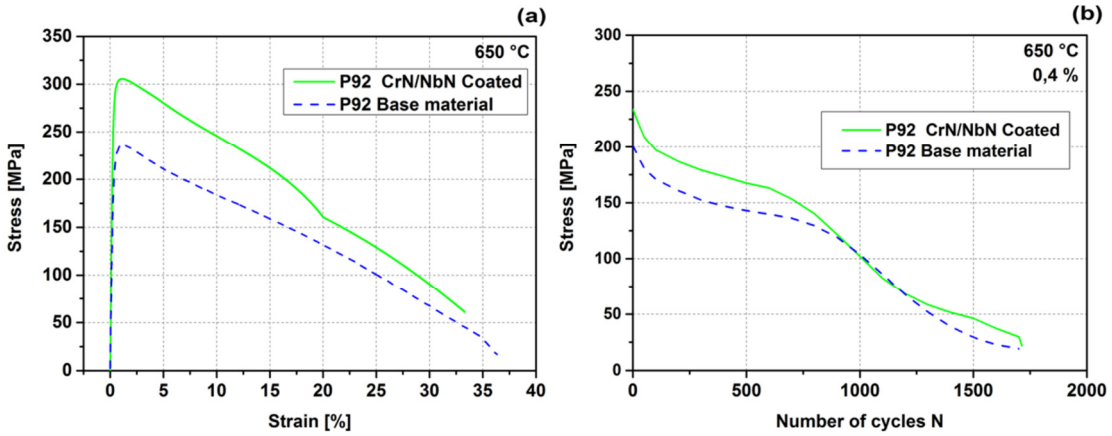

Figure 7: Mechanical tests of the uncoated and the coated P92 base material (low Nb CrN/NbN coating) at 650 °C: a) Stress-strain diagram, b) Cyclic stress response of the coated specimen and P92 base material at 650 °C and a constant strain amplitude of 0.4 %.

The results of the low cycle fatigue tests at 650 °C are presented in Figure 7b. The coated sample and the base material sustained an approximately identical number of cycles to failure (N_f) of 1.700 cycles and 1.712 cycles respectively. A similar behaviour was observed with regard to the cyclic stress response as well. In particular, the starting stress amplitude $\Delta\sigma_{(N1)}$ and the half-life stress amplitude $\Delta\sigma_{(Nf/2)}$ were comparable for both samples. The P92 base material had $\Delta\sigma_{(N1)}$ of 200 MPa and $\Delta\sigma_{(Nf/2)}$ of 126 MPa which resulted in a stress drop of 37 %. The coated sample has slightly higher values of $\Delta\sigma_{(N1)}$ = 235 MPa, $\Delta\sigma_{(Nf/2)}$ = 133 MPa and a resulting stress was about 43 % after the fatigue exposure. These results confirm unequivocally that the coating procedure causes no significant change in the base material. A wider program of experiments and parallel tests at different strain amplitudes will cover the whole range of fatigue modes.

Figure 8 shows the resulting creep curves (figure 8a) and the corresponding strain rate (figure 8b) at 650 °C and 120 MPa of creep load. As shown in the left-hand diagram both samples exhibit the typical three stages of creep, such as primary stage, secondary steady state creep stage and tertiary accelerating creep stage. The first stage is characterised by a strong decrease

of the strain rate due to multiplication of dislocations. The steady state creep stage shows a certain range of minimum creep rate, which is attributed to the dynamic balance between hardening and microstructural recovery (Figure 8b). The third creep stage is dominated by the formation and growth of creep pores, which first lead to a rapid increase of strain rate and finally to creep failure. The average minimum creep rate during the steady state creep stage of the uncoated base material is about 17.6 $x10^{-6}$ $1s^{-1}$ which exceeds the minimum creep rate of the coated sample (12.1 x 10^{-6} $1s^{-1}$). This slightly accelerated creep behaviour of the base material results in a relatively shorter creep life of 564 h. In comparison, the coated sample exhibits a time to fracture of 908 h, which is an increase of approximately 61 %. These results unambiguously demonstrate that the coating process leads to improved creep properties of the system. It can be summarised that in all three tests carried out in this research such as Stress-strain, Cyclic stress and Creep test the mechanical properties of the base material after coating remained unchanged. This exceptional response of the coating/substrate system to various types of mechanical loads can be attributed to two main qualities: namely the special properties of the coating/ substrate interface achieved by the HIPIMS surface pre-treatment and the hindered inter-diffusion of Hydrogen into the substrate material due to the barrier properties of the coating as discussed in 3.3. Both qualities hinder the crack initiation and crack propagation in the substrate material thus resulting in preservation of its properties under mechanical load after the coating deposition.

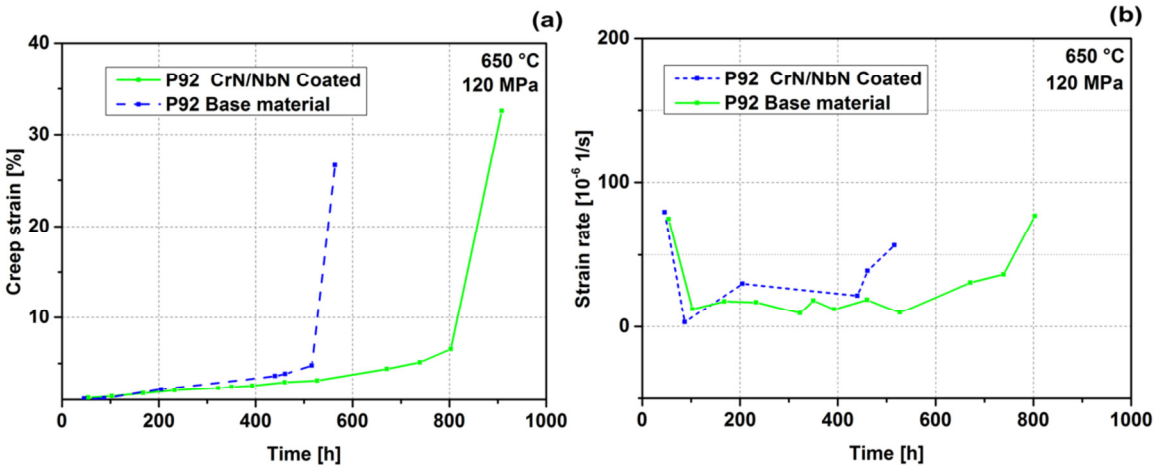

Figure 8: (a) Creep curves and (b) strain rate dependency (right) of the coated and uncoated specimen, tested at 650 °C and 120 MPa.

3.6 *Water Droplet Erosion Test Results*

Recent theories describing the effect of a water droplet impacting a solid surface in aero engines, distinguish between three shock waves; namely a compressional wave, followed by a shear wave succeeded by a Rayleigh wave [23].

The pressure *P* created during such impact is given by the water hammer equation [24] (Eq. (2)),

$$P = \rho_o c_o V_o, \quad (2).$$

where ρ_o is the density of the water, c_o is the speed of sound in the undisturbed liquid and V_o is the impact velocity.

In aviation studies, for the case of water droplet erosion, the parameter 'Damage Threshold Velocity (DTV)' represents the lowest velocity, which could theoretically cause damage in the target material. This parameter was successfully linked to the properties of the target material by Evans *et al.* [25] who showed that the DTV is proportional to the fracture toughness of the target material and the Rayleigh wave velocity on it. The theoretical expression for the DVT is shown in equation (3),

$$Vdt \approx 1.41 \left(\frac{{K_{ic}}^2 . C_R}{{\rho_w}^2 . C_w}\right)^{1/3} \quad (3).$$

where V_{DT} denotes the DVT, ${K_{ic}}^2$ the fracture toughness of the target material, C_R the Rayleigh wave velocity on the target material, ρ_w the density of water, C_w the compressional wave speed in water, and d_w is the diameter of the water droplets.

Achenbach *et al* [26], who showed that C_R is proportional to the Young's modulus, E and therefore the hardness of the impacted material, demonstrated further dependency of *DVT* on the target material properties.

The above theory clearly defines the fracture toughness and hardness as two of the most influential material properties for high water droplet erosion resistance. When initially introduced, superlattice or nanoscale multilayer structured PVD coatings were extremely attractive as their hardness could exceed 40 GPa and classify them as superhard. The nature of these high hardness values has been discussed in context of a specific layer thickness which was tailored to arrest the diffusion of crystalline defects due to the energy barrier properties of the interfaces between the individual layers, and on the difference of the shear modulus of the materials involved, (the superhardening effect) [27]. Following further research, unique properties of the layered structures such as crack deflection at the interfaces and their role as sites for elastic energy dissipation were also added to the established mechanisms responsible for the enhancement of the mechanical properties [28]. Recently, advanced *in-situ* micromechanical cantilever bending tests, used for precise evaluation of the fracture toughness on free-standing hard PVD films, elucidated this effect more clearly [29]. Furthermore, it was shown that in superlattice structured coatings a significant fracture toughness enhancement can be achieved (for e.g. by factor of two for the TiN/CrN system) in a way similar to the superhardeneing effect reported for these structures [30]. The synergy

between superhardness and a special crack propagation mechanism render these artificially made nanolaminated materials as the toughest amongst all other PVD coatings.

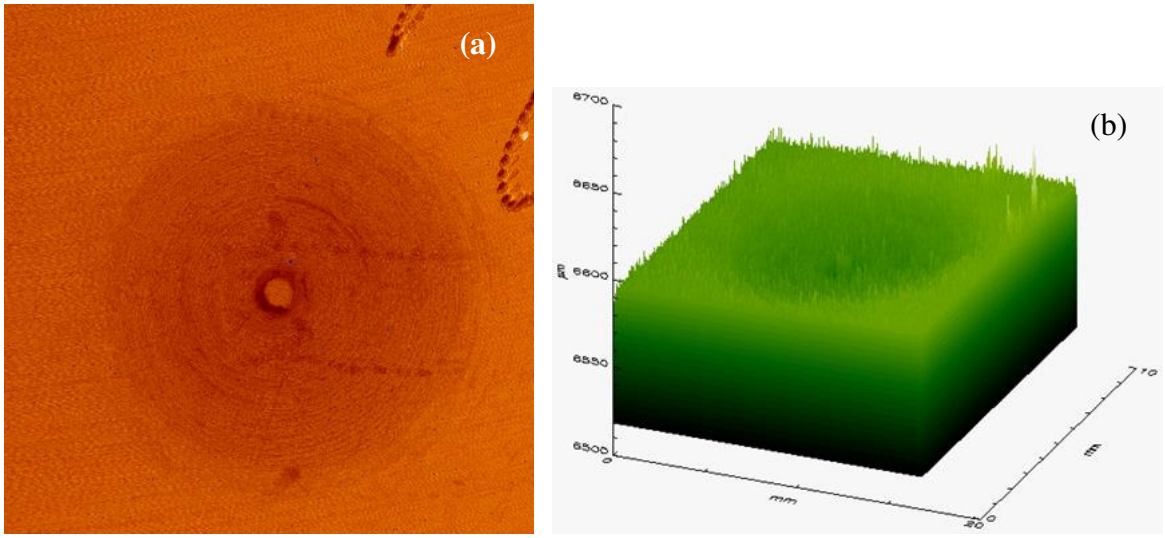

Figure 9: Droplet erosion test results (a) 2-D Surface Plot (step size in x- and y-direction is 0.1 mm) (b) 3D Plot x- and y-steps 0.02 mm.

In this study, low Nb CrN/NbN coating was investigated for its droplet erosion resistance. After $2.4x10^6$ impacts at a pressure of 9 bar, no measurable weight loss was detected. SEM images (not included) of the impacted area of the surface showed that only a gentle polishing had taken place. The surface morphology after the erosion test resembled largely the original morphology as shown in figure 3a. The excellent droplet erosion resistance observed can be attributed to their very high hardness of 35 GPa, high Young's modulus of 392 GPa and very high toughness due to the layered structure on a nanoscale. A 2D surface plot revealed the formation of a shallow circular depression at the targeted surface area, figure 9a. Using 3D plots and profilometry, the depth of the depression was found to be around 20 µm, figure 9b. It can be speculated that the depression was created by deformation of the substrate material beneath the area of the sample which was impacted by the water jet. Crucially, no coating delamination or cracks were observed under the post-test SEM imaging, which demonstrated

the exceptionally high coating adhesion and high impact load resistance of the coating achieved by the HIPIMS technology.

4. Conclusions:

1. The employment of the novel HIPIMS technology resulted in production of a CrN/NbN nanoscale multilayer coating with enhanced adhesion (critical scratch adhesion value of Lc_2= 80N) and very high coating density as shown by FIB SEM and XTEM analyses.

2. The enhanced protection mechanism (oxidation resistance) of the CrN/NbN coatings utilising nanoscale multilayer structure can be described as one of formation of a protective Cr and Nb containing oxide scale, as well as hindered elemental transport through the coating due to the barrier properties of the interfaces between the individual nanolayers of CrN/NbN as confirmed by cross section SEM and EPMA elemental distribution mapping.

3. The thermodynamic simulation of the CrN/NbN-steam system predicted the formation of two stable oxides namely, Cr_2O_3 and Nb_2O_5, and was confirmed by XRD analyses. The calculations showed that the Gibbs free energy, ΔG for formation of Nb_2O_5, (ΔG = - 29.8 kJ/mol) is much lower compared to that of Cr_2O_3, (ΔG = - 25.2 kJ/mol), indicating that the formation of Nb_2O_2 is more favorable during steam oxidation of CrN/NbN.

4. The oxidation resistance of nanoscale multilayer structured CrN/NbN exposed to high temperature (600^{o}C) steam atmosphere depends on the Nb content in the film. The experiments showed that the low Nb containing coatings, (Cr/Nb= 2.44) were superior to the CrN/NbN coatings with higher Nb content, (Cr/Nb= 1.16).

5. The crack formation in the oxide scale during the steam oxidation process was attributed to the volume expansion of the individual oxides and the Hydrogen embrittlement. As the specific volume of Nb_2O_5 is 12% larger than that of the Cr_2O_3, it is expected that the crack development process will be dominated by the amount of the Nb_2O_5 formed and therefore the Nb content in the film.

6. THERMO-CALC simulation predicted that in addition to the purely oxidising gaseous compounds, a certain amount of Hydrogen both in atomic and molecular form can be found in the steam. GDOES depth profile analysis confirmed that the Hydrogen inter-diffuses in the coating causing excessive brittle failure as observed by SEM. Importantly however, GDOES depth profile analysis also revealed that CrN/NbN provided a reliable barrier against Hydrogen incorporation in the substrate material.

7. Unlike other state-of -the-art PVD technologies, HIPIMS does not have an adverse effect on the mechanical properties of the substrate material. This was demonstrated in a number of high temperature tests at 650^{o}C.

The coated sample exhibited enhanced ultimate tensile strength (UTS) values of 307 MPa and yield strength (YS) values of 291 MPa, compared to those of the base material, 229 MPa (UTS) and 222 MPa (YS).

Low Cycle Fatigue at a constant strain amplitude of 0.4% showed an approximately identical number of cycles to failure N_f of 1700 cycles and 1712 cycles for the coated and uncoated samples respectively.

High Temperature Creep tests at 120MPa creep load, revealed improved creep properties for the coated samples. The creep rate for the coated samples, (12.1×10^{-6} $1s^{-1}$) was lower compared to that of the uncoated base material, 17.6×10^{-6} $1s^{-1}$, whereas time to fracture of 908 hours was longer compared to 564 hours for the uncoated base material.

8. A specialized test rig was used to evaluate the protection properties of the coating against water droplet erosion attack. The coating showed high resistance against water droplet erosion. After 2.4 x 10^6 impacts at a 9 bar pressure no measurable weight loss was detected.

9. The synergy between advanced coating nanostructure and the application of the High Power Impulse Magnetron Sputtering deposition technology projected CrN/NbN as a potential candidate for the protection of steam turbine blades as it possesses the whole package of functional properties required for this application.

Acknowledgements:

This work has been carried out within FP7 EC funded project "Production of Coatings for New Efficient Clean Coal Power Plant Materials", POEMA, Grant agreement 310436. The financial support of the EC and the intellectual support of all partners are deeply acknowledged. Mr. Paul Allender and Mr. Gary Robinson, Sheffield Hallam University, are kindly acknowledged for their support in providing TEM facilities and technical support respectively.

References:

[1] J. White, Analysis of supercritical steam cycle, Gilbert Commonwealth, 1995.

[2] Jianfu Hou, Bryon J Wicks, Ross A Antoniou, *Eng. Failure Anal.* 9 (2) (2002) 201–21.

[3] D.P Walls, R.E Delaneuville, S.E Cunningham, *J. Eng. Gas Turbines Power* 119 (1997) 143–146.

[4] C Persson, P.O Persson, *J. Mater. Eng. Perform.* 2 (4) (1993) 565–569.

[5] T.Sourmail, Coatings for turbine blades, University of Cambridge, www.msm.cam.ac.uk

[6] A. P. Ehiasarian, "Fundamentals and applications of HIPIMS," in Plasma surface engineering research and its practical applications, R. Wei. Trivandrum, India, Research Signpost (2007) 35-86, ISBN 978-81-308-0257-2.

[7] A. P. Ehiasarian, R. New, W.-D. Münz, L. Hultman, U. Helmersson, V. Kuznetsov, Vacuum 65 (2002) 147-154.

[8] P. Eh. Hovsepian, D. B. Lewis, W.-D. Münz, *Surf. Coat. Technol.* 133-134 (2000) 166-175.

[9] Y. P. Purandare, A. P. Ehiasarian and P. Eh. Hovsepian, *J. Vac. Sci. Technol.* A 26, 2(2008) 288-296.

[10] M. M. Stack, Y. Purandare and P. Eh. Hovsepian, *Surf. Coat. Technol.* 188-189 (2004) 556-565.

[11] P.Eh. Hovsepian, D.B. Lewis, Q. Luo, W.-D. Münz, M. Meyer, *Surface Engineering*, Euromat Vol. 11 (1999) 41-46 proceedings, edited by H. Dimigen.

[12] C. Nico, T. Monteiro, M.P.F. Graça, *Prog. Mater. Sci.* 80 (2016) 1–37.

[13] R.Smith, *J. Less-Common MET.* 2 (1960) 191- 206.

[14] P. Eh. Hovsepian , A.P. Ehiasarian , Y.P. Purandare, B. Biswas, F.J. Perez, M.I. Lasanta, M.T. de Miguel, A. Illana, M. Juez-Lorenzo, R. Muelas, A. Agüero, *Mater. Chem. Phys.* 179 (2016) 110-119.

[15] A.P. Ehiasarian, P.Eh. Hovsepian, W-D. Münz Patent US7081186 B2 (25 Jul 2006), EP1260603 A2 (27 Nov 2002), DE10124749 A1 (28 Nov 2002).

[16] B. Chapman, in Glow Discharge Processes. John Wiley & Sons, USA, 1980.

[17] T. Hurkmans, D.B. Lewis, H. Paritong, J.S. Brooks, W.D. Munz, *Surf. Coat. Technol.* 114 (1999) 52–59.

[18] P.Eh. Hovsepian, D.B. Lewis, Q. Luo, A. Farinotti, *Thin Solid Films* 488 (2005) 1 – 8.

[19] D.B. Lewis, Q. Luo, P.Eh. Hovsepian, W.-D. Münz, *Surf. Coat. Technol.* 184 (2004) 225–232.

[20] A. P. Ehiasarian1, A. Vetushka, Y. Aranda Gonzalvo, G. Sáfrán, L. Székely, and P. B. Barna, *J. Appl. Phys*. 109 (2011) 104314.

[21] Thermocalc Software, 1995-2003. Foundation of computational thermodynamics, Stockholm, Sweden.

[22] Database, Scientific Group Thermodata Europe. http://www.thermocalc.com (accessed March 2017).

[23] O. Gohardani, *Prog. Aerospace Sci*. 47 (4) (2011) 280-303.

[24] F.J. Heymann, *J. Appl. Phys*. 40 (13) (1969) 5113-5122.

[25] A.G. Evans, M.E. Gulden, M. Rosenblatt. Rockwell International Thousand Oaks Calif Science Center, 361 (1978) 122-136.

[26] J. Achenbach, *Wave Propagation in Elastic Solid*s, North-Holland Serries in Applied Mathematics and Mechanics, 361(1973) 425.

[27] S.A. Barnett, Physics of Thin Films, Vol.17. edited by M.H. Frankombe and J.L. Vossen, (Academic Press, Boston, 1993).

[28] H. Hollek and V. Schier, *Surf. Coat. Technol.* 76 (1995) 328-336.

[29] A.Riedel, R. Daniel, M. Stefenelli, T. Schöberl, O. Kolednik, C. Mitterer and J. Keckes. Scripta Materialia 67 (2012) 708-711.

[30] R. Hann, M. Bartosik, R. Soler, C. Kirchlechner, G. Dehm, P. H. Mayerhofer. *Scr. Mater*. 124 (2016) 67-70.

Figure Captions

Figure 1. X-ray diffraction patterns of the CrN/NbN coatings (a) LAXRD pattern used for calculation of the bi-layer period. (b) Bragg-Brentano θ-2θ scan results.

Figure 2. Scanning electron microscope images of CrN/NbN coating on P92 substrate: (a) surface morphology, (b) FIB cross-section image.

Figure 3. Bright field STEM (a) low magnification cross-section of the coating showing base layer and adjacent coating (b) high magnification showing the multilayers (c) high resolution TEM image showing the microstructure at an atomic scale [20].

Figure 4. Main phases developed from the low Nb CrN/NbN coating exposed to 100% steam atmosphere at: (a) 1bar pressure, (b) 50 bar pressure.

Figure 5. SEM cross-sectional image and EPMA elemental distribution map of CrN/NbN with high Nb content, Cr/Nb= 1.16 exposed to 600^{o}C pure steam atmosphere at 50 bar pressure for 1000 h.

Figure 6. GDOES depth profile of steam oxidized low Nb CrN/NbN coating.

Figure 7. Mechanical tests of the uncoated and the coated P92 base material (low Nb CrN/NbN coating) at 650 °C: a) Stress-strain diagram, b) Cyclic stress response of the coated specimen and P92 base material at 650 °C and a constant strain amplitude of 0.4 %.

Figure 8. (a) Creep curves and (b) strain rate dependency (right) of the coated and uncoated specimen, tested at 650 °C and 120 MPa.

Figure 9. Droplet erosion test results (a) 2-D Surface Plot (step size in x- and y-direction is 0.1 mm) (b) 3D Plot x- and y-steps 0.02 mm.